

# Computational Fluid Dynamics-Based Design Optimization for an Implantable Miniature Maglev Pediatric Ventricular Assist Device

## Jingchun Wu

Ph.D., Chief Scientist  
LaunchPoint Technologies, Inc.,  
5735 Hollister Ave., Suite B,  
Goleta, CA 93117  
e-mail: jwu@launchpnt.com

## James F. Antaki

Ph.D., Professor  
Department of Biomedical Engineering  
and Computer Science,  
Carnegie Mellon University,  
700 Technology Drive, Suite 4321,  
Pittsburgh, PA 15213  
e-mail: Antaki@andrew.cmu.edu

## Josiah Verkaik

Senior Mechanical Engineer  
e-mail: jverkaik@launchpnt.com

## Shaun Snyder

Senior Electrical Engineer  
e-mail: ssnyder@launchpnt.com

## Michael Ricci

Vice President of Engineering  
e-mail: mricci@launchpnt.com

Launch Point Technologies, Inc.,  
5735 Hollister Avenue, Suite B,  
Goleta, CA 93117

*Computational fluid dynamics (CFD)-based design optimization was applied to achieve the finalized design of the PediaFlow<sup>®</sup> PF4, a magnetically levitated rotodynamic pediatric ventricular assist device. It features a streamlined blood-flow path with a single annular fluid passage between the rotor and the stationary housing. The resulting impeller is composed of a first-stage mixed-flow section having four blades at the conical nose region followed by a second-stage fully axial-flow section with three blades within the annular gap region. A stator with three inwardly-directed vanes is provided at the conical tail region to recover pressure and straighten the flow. CFD predictions of head and efficiency characteristics agreed remarkably well with the validation experimental data: with overprediction of head by <7 mmHg over the entire operational range and a slight overprediction in best efficiency by ~1%. The new optimized PF4 extended the maximum flow range of the previous PF3 device by more than 100% to over 2.3 liter per minute (LPM) for the same range of operating speeds, and doubled the maximum hydraulic efficiency to ~27%. Evaluation of hemolysis was performed by a Lagrangian particle-tracking technique with analysis of regional contributions to the overall blood damage. The simulation revealed that hemolysis increases with an increase in both the flow rate and rotor speed but not necessarily with just an increase in flow rate at a constant rotor speed. At the flow rate of 1.0 LPM and a head of 138 mmHg, PF4 has a hemolysis index of 0.0032 compared to 0.0058 produced by PF3 at the same flow rate with a head of 48 mmHg. Numerical simulation of radial fluid forces performed by the CFD model with an eccentric rotor revealed the presence of negative fluid stiffness that was monotonically related to both flow and speed. Finally, conjugate heat transfer analysis predicted temperature rise adjacent to the motor to be inversely proportional to the length, but not exceeding ~2°C over the intended range of operation. In conclusion, CFD-based design optimization greatly expedited and facilitated the completion of the PediaFlow<sup>®</sup> flow path and contributed to the system-wide optimization to produce a miniature maglev pump with exceptional hemocompatibility. [DOI: 10.1115/1.4005765]*

*Keywords: pediatric ventricular assist device, left ventricular assist device (LVAD), computational fluid dynamics, optimization, hemolysis, radial fluid stiffness, heat transfer, two-stage impellers*

## 1 Introduction

According to recently available statistics, approximately 36,000 new cases of congenital heart disease (CHD) occur each year [1]. Of these, several studies suggest that 9200, or 2.3 per 1000 live births, require invasive treatment or result in death in the first year of life [2]. The very limited options available to treat ventricular failure in these infants and young children have motivated us to develop the PediaFlow<sup>®</sup> ventricular assist system, which features a miniature rotodynamic blood pump having a magnetically levitated impeller and streamlined blood flow path. It is intended to be fully implantable, providing chronic (up to 6 months) circulatory support from birth to 2 years of age (3 kg to 15 kg body weight) with a nominal pressure rise of ~100 mmHg for the flow range of 0.3~2.3 L/min. By consideration of the hemodynamic requirements of this population [3], a nominal design point of 1.5 LPM

with a target pressure rise of 100 mmHg was chosen for the design procedure. An important design requirement is the need for optimizing and miniaturizing the flow path to maximize hemodynamic performance while minimizing shear-stress induced blood trauma.

A unique feature of magnetically levitated axial-flow blood pumps in general, and the PediaFlow<sup>®</sup> in particular, is a continuous annular fluid gap between rotor and housing. The dimensions of this gap are limited by the requirements for magnetic stiffness and motor efficiency, but must be sufficiently large to permit desired flow of blood and to avoid excessive shear stress and other flow disturbances. When shared with the impeller blades, a narrow annular flow gap generally necessitates greater rotational speeds to generate sufficient pressure rise and flow rate. However, the combination of small gap and high speed can be a formula for blood cell damage without sufficient optimization of flow path geometry including the blade profiles.

Because of design tradeoffs such as these, which span across several subsystems of the PediaFlow<sup>®</sup> (electromagnetics, heat transfer, rotordynamics, etc.), our group has adopted a numerical, multidisciplinary approach to optimization. With regard to the

Contributed by the Fluids Engineering Division of ASME for publication in the JOURNAL OF FLUIDS ENGINEERING. Manuscript received August 11, 2011; final manuscript received January 3, 2012; published online March 27, 2012. Assoc. Editor: Z. C. Zheng.

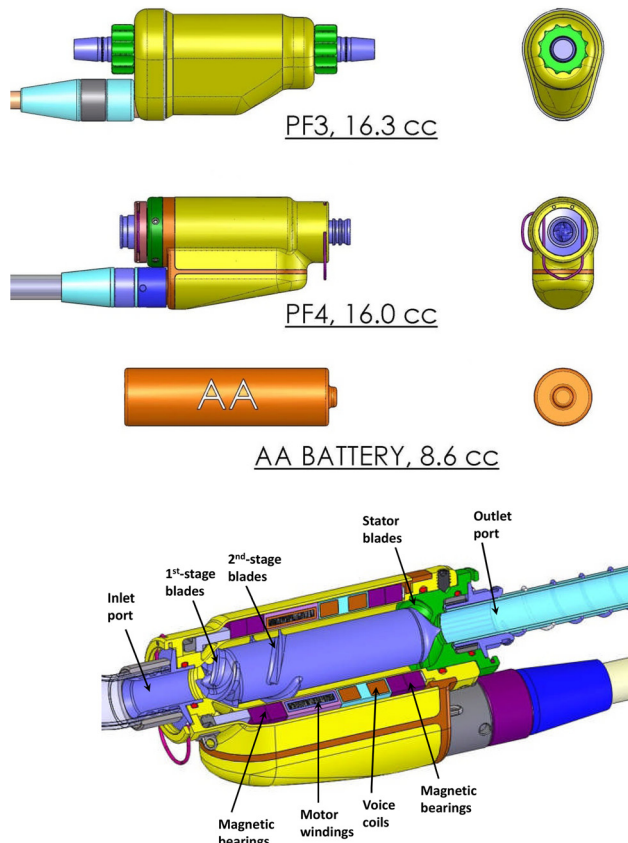


**Fig. 1** Two generations of the PediaFlow<sup>®</sup> ventricular assist device: PF3 and PF4. Cutaway (bottom) shows critical internal components of PF4.

flow path, we employed a CFD-based design optimization system developed by Wu et al. [4,5] that integrates a robust and flexible inverse blade design tool, automatic mesh generators, parameterized geometry models, and mathematical models of blood damage, integrated with commercial CFD packages.

The PediaFlow<sup>®</sup> pump has evolved over four generations, denoted as PF1, PF2, PF3, and PF4. The PF3 evolved from its predecessor (PF2, [6]) by the realization that the rotor can operate above its rotordynamic critical rotational speed, which reduced the requirement for magnetic suspension stiffness. This, in turn, permitted a relatively larger annular gap; hence, smaller rotor diameter. Although PF3 demonstrated excellent *in vivo* biocompatibility over 72 days [7], adverse fluid–structure interaction caused an unstable operational range greater than 0.8 L/min and 18,000 revolutions per minute (rpm). This study describes the use of the aforementioned CFD-based design optimization tools for overcoming this limitation and thereby expanding the operating range and improving hydrodynamic performance in transitioning from the PF3 to a frozen PF4 design, as illustrated in Fig. 1.

## 2 Materials and Methods

**2.1 PediaFlow<sup>®</sup> (PF4) Blood Path.** To increase the flow capacity and upgrade the performance of the PF3 pump, yet maintain the suspension system and the main geometric dimensions such as rotor diameter and annular fluid gap, a novel two-stage impeller was implemented for the PF4 design, consisting of a first-stage mixed-flow type section with four blades followed by a second-stage axial-flow type section having three blades (see Fig. 2). The first-stage mixed-flow impeller is located in the inlet transitional conical region of the rotor similar to the position of that in PF3 with a purely one-stage mixed-flow impeller [6,7]. The second-stage

axial-flow type impeller is positioned within the annulus downstream of the first stage. Both stages are semiopen impellers, which have the blade tip clearances between the lengthwise upper surfaces of the rotational blades and the stationary housing. A stationary stator stage has three inwardly-directed vanes with a tiny clearance between the vane tip surface and the rotor. The stator provides pressure recovery at the tail section and guides the blood to discharge axially with low disturbance. Both the first- and second-stage impeller blades were designed and optimized with our custom-developed inverse design CFD software reported previously [4,5]. The optimization assured that the leading edge blade angles of the second stage along each stream-surface from hub to shroud were matched to the incident blood flowing from the first stage at the design point and its nearby operational points. The wrap angles of both stages were maintained as small as possible to reduce boundary layer effects. The inverse design tools were further applied to optimize the three-dimensional profiles of the stator vanes to assure confluence with the incident flow along each stream-surface. The trailing edge angles of the stator vanes were specified at approximately 90 deg to optimally recover the dynamic head.

One important consideration to assure high accuracy is the integrity of the numerical mesh. Figure 2 illustrates a representative multiblock structured surface mesh, generated with our internally developed mesh generator using the elliptic generation systems [8]. Particular attention was paid to assure orthogonality to the wall surfaces, quasi-orthogonality within each cell, and complete continuity through all the block-to-block interfaces. A refined clustering O-grid was prescribed around all blade and vane profiles to capture the steep velocity gradients near their surfaces (see Fig. 2(b)). Because of the particular importance of the flow within the clearances of the impeller blade and stator-vane tip, 12 nodes were distributed across these clearances, clustered near the surfaces. The inflow cannula with a 45 deg elbow and the outflow graft with 90 deg elbow were also included in the computational domain using a multiblock structured butterfly-type grid (see Fig. 2(c)). For all the turbulence simulations, the grid independency check was conducted to ensure that the monitored field variables such as pressure and velocity, at several representative points of the two sets of meshes differ by less than 2%. The resulting mesh was comprised of approximately 2.5M cells for the entire pump model based on the grid-sensitivity studies.

Blood was treated as a Newtonian fluid with the asymptotic viscosity and density prescribed at 0.0035 Pa-s and 1040 kg/m<sup>3</sup>, respectively. Additional simulations were performed with values more closely corresponding to nominal values for the ovine model used for our *in vivo* studies (0.00244 Pa-s and 1076 kg/m<sup>3</sup>). Numerical simulation of the Navier-Stokes equations was accomplished using a commercial CFD solver (CFX, ANSYS, Inc., Canonsburg, PA). The representative Reynolds number at nominal flow condition (1.5 L/min, 16,000 rpm) was approximately 30,120 based on the second-stage impeller outlet diameter and the rotor speed ( $Re = \rho u_2 D_2 / \mu$ ) [9]. Accordingly, a shear stress transport (SST) model [10,11], typically prescribed for turbulence of the low Reynolds number, was selected for all the simulations. The near-boundary first-node grid was automatically calculated and controlled by the mesh generator so that the dimensionless boundary layer thickness  $Y^+$  was less than 2.0 for all the conditions simulated. The “frozen rotor” method was applied to couple the interfaces between rotational and stationary domains [11]. Based on Bludszuweit’s assumption of linear accumulation of shear at different loading levels [12], blood damage was evaluated with the power-law functions as suggested by Song et al. by regression of experimental data from Heuser et al. [13] using a Lagrangian particle-tracking technique as described in our previous report [14].

**2.2 Experimental Validation.** To validate CFD results prior to implementation of the maglev system, hydrodynamic performance testing and flow visualization were conducted using a transparent replica of the optimal pump geometry in which the rotor

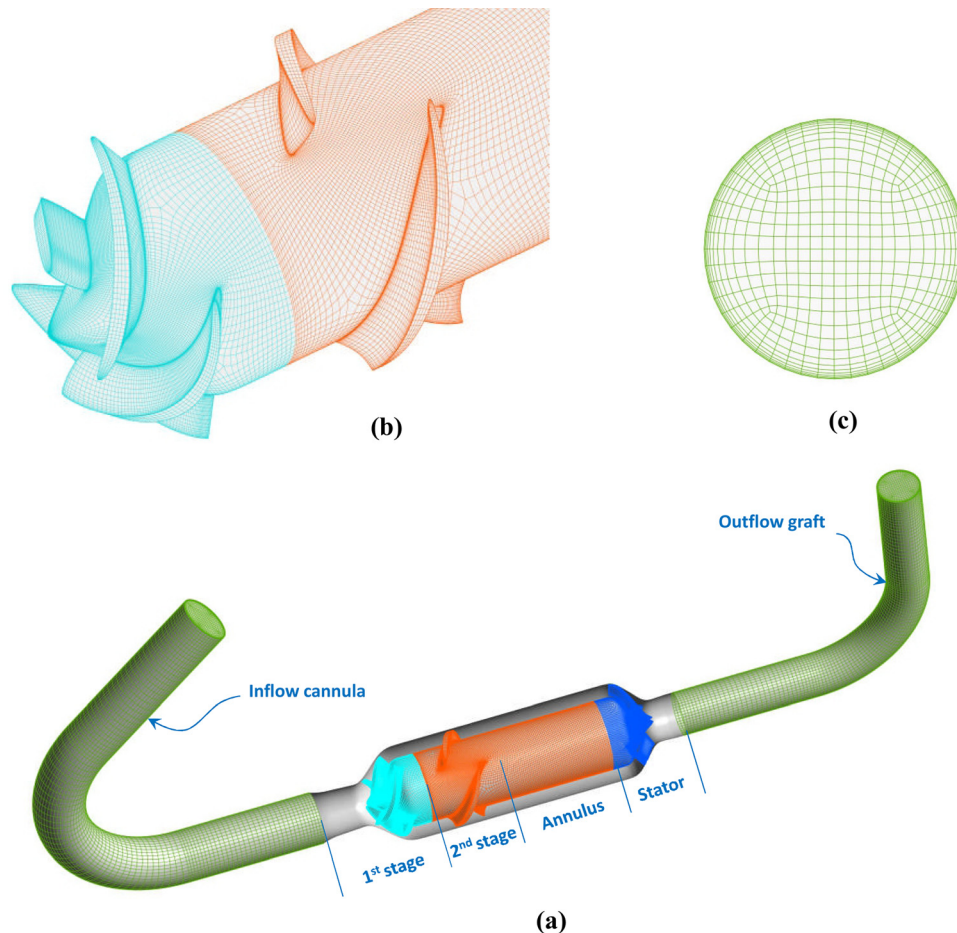


**Fig. 2 High-quality multiblock structured CFD surface mesh generated by custom-developed automatic elliptic generation system with boundary orthogonality and complete continuity at interfaces. (a) Entire PediaFlow<sup>®</sup> PF4 flow path. (b) Refined clustering O-grid around blade profiles. (c) Butterfly-type grid for cross sections of inflow cannula and outflow graft.**

was supported by mechanical contact bearings (see Fig. 3(a)). The experimental apparatus was not subject to the effects of destabilizing force as exhibited in the magnetic suspension. Accordingly, for validating accuracy of CFD analyses, a separate series of simulations were performed in which the exact dimensions and details of the contact bearings were replicated (see Fig. 3(b)). All experiments reported in this paper were performed with a blood analog composed of glycerol and saline with a density of  $1076 \text{ kg/m}^3$  and dynamic viscosity of  $0.00244 \text{ Pa}\cdot\text{s}$  for comparison to *in vivo* testing data performed with sheep. For the experimental data, the pressure head was measured via the inlet and outlet pressure ports using piezoelectric pressure transducers (TruWave, Edwards Lifesciences LLC) and the volumetric flow rate was measured with an ultrasonic flow-meter (Transonic Systems Inc., Ithaca, NY). The pressure and flow sensors were calibrated prior to testing to maintain an accuracy of less than or equal to  $1 \text{ mmHg}$  and  $2\%$ , respectively.

**2.3 Fluid Stiffness Modeling.** To investigate the influence of unbalanced radial loading because of fluid dynamic forces, which limited the maximum speed and flow capacity of the PF3 design, an additional CFD model of the PF4 was constructed in which the rotor was eccentrically displaced from the central axis of the bore. Based on the existing multiblock structured mesh at the coaxial symmetrical position as shown in Fig. 2, the mesh movement and adaptation corresponding to each radial displacement of the rotor were recalculated to maintain the same mesh structure and quality [8].

**2.4 Conjugate Heat Transfer Analysis.** A previous heat transfer analysis of the earlier PediaFlow<sup>®</sup> design using a reduced

order analytical model determined the temperature rise in the blood to be  $\sim 1^\circ\text{C}$  [15]. To increase the accuracy for the current study, conjugate heat transfer was employed [11] as shown in Fig. 4. For simplicity, the heat loss from the motor was assumed to be  $2 \text{ W}$  for the two different motor lengths of  $3.0$  and  $6.0 \text{ mm}$ , and the pump housing was represented by a shell of  $0.175\text{-mm}$ -thick titanium alloy (Ti6Al4V). Heat transfer in the fluid was simulated by a total energy equation coupled to the Navier-Stokes equations with SST turbulence model. Continuity constraints were enforced at the interface between the titanium shell and the flowing blood.

### 3 Results

For comparison to experimental data, simulation results shown in Figs. 6 and 7 were performed with an analog blood density of  $1076 \text{ Kg/m}^3$  and viscosity of  $0.00244 \text{ Pa}\cdot\text{s}$ . All of the other results presented in this paper correspond to blood density of  $1040 \text{ Kg/m}^3$  and viscosity of  $0.0035 \text{ Pa}\cdot\text{s}$ . The predicted velocity vectors on mid-span blade-to-blade surface through the first- and second-impeller region at nominal design point ( $Q=1.5 \text{ LPM}$  and speed =  $16,000 \text{ rpm}$ ) and the off-design condition ( $Q=2.3 \text{ LPM}$  and speed =  $16,000 \text{ rpm}$ ) are illustrated in Figs. 5(a) and 5(b), respectively. Also shown are the pathlines through PF4 entire flow path at the design point (see Fig. 5(c)). Because of the use of our inverse design tools with high-performance hydrofoil for all the impeller and stator blades, the velocity vectors exhibited smooth flow field that was confluent between the first and second stages without any separation or vortices throughout the entire impeller region over a wide operational range as illustrated in

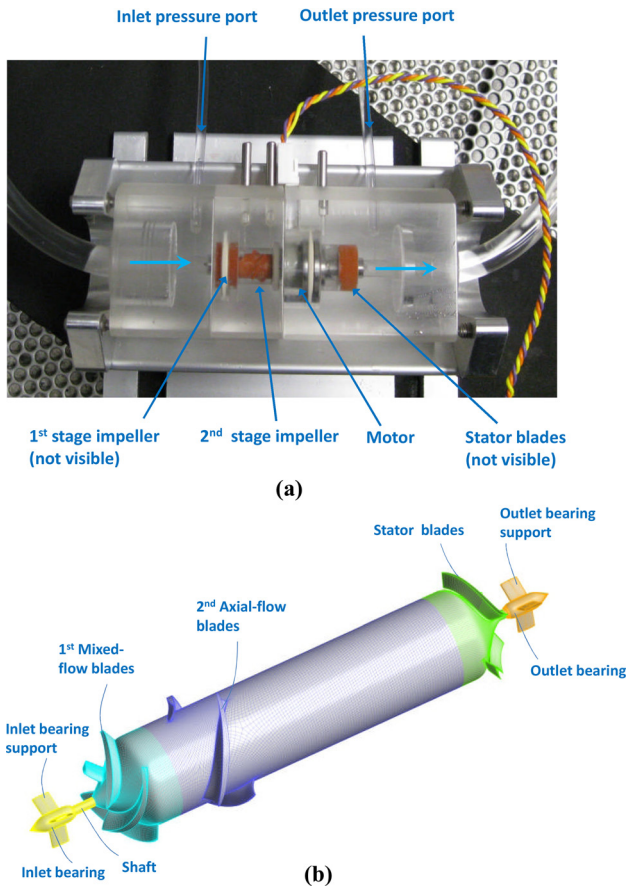


**Fig. 3** PediaFlow<sup>®</sup> PF4 flow validation fixture. (a) Experimental assembly. (b) Corresponding CFD model with high-quality multi-block structured surface mesh.

Figs. 5(a) and 5(b). Figure 5(c) displays a subset of the 6000 pathlines from inflow cannula to outflow graft used for computing blood trauma. These pathlines also present a smooth flow pattern with the exception of some disturbance observed in the outflow graft downstream of the three-vane stator stage. Theoretically, the observed swirling flow may be reduced by the addition of stator vanes. However, in practice, it is precluded by manufacturing limitations because of their high curvature, twist, and small pitch. Moreover, the addition of the stator vanes would also correspondingly increase the “wet area” of the flow path, which may induce extra hemolysis especially at larger flow rates as discussed in the

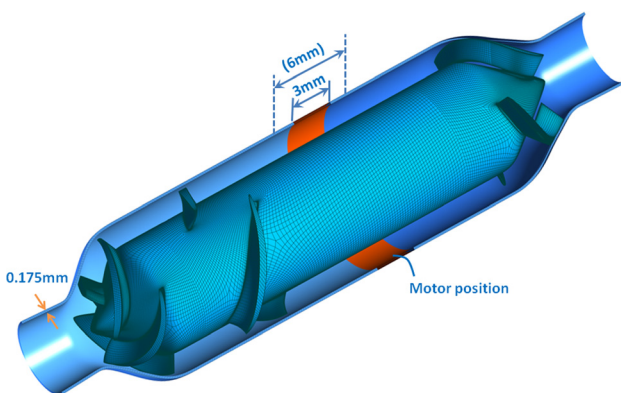


**Fig. 4** CFD model for coupled solid-fluid thermal analysis. Shell of titanium alloy (Ti6Al4V) was included with a thickness of 0.175 mm, and two motor lengths of 3.0 mm and 6.0 mm were modeled.

following section. Therefore, the best compromise was found with three stator vanes for the current PF4 design.

**3.1 Characteristic Performance.** The predicted head-flow ( $H-Q$ ) characteristics by CFD for the PF4 flow validation fixture (Fig. 3) agreed very well with the experimental data. The maximal overprediction in head was less than 7 mmHg over the entire range of flow rates and rotor speeds (see Fig. 6). The predicted efficiency-flow ( $\eta-Q$ ) characteristics also agreed well with the experimental measurements over the full range of flow and speed (see Fig. 7). The best efficiency predicted by CFD was  $\sim 1\%$  greater than that determined experimentally. Compared to previous PediaFlow<sup>®</sup> PF3 experimental data obtained from an identical flow fixture (superimposed in Figs. 6 and 7), the optimized PF4 consistently generated greater head at reduced rotor speed for a given flow rate. The useful flow capacity was also dramatically increased from 1.0 to over 2.3 LPM (see Fig. 6) with no increase to the overall volume of the pump system. The corresponding improvement in maximum efficiency illustrated in Fig. 7 is approximately twice that of PF3.

Figure 8 illustrates the difference in CFD-predicted performance between the magnetically suspended configuration (Fig. 2) and the flow validation test fixture having mechanical support bearings (Fig. 3). Because of the flow disturbance of the mechanical bearings and supports, there was a notable reduction in both head (Fig. 8(a)) and efficiency (Fig. 8(b)) particularly at the greater flow range, which deviated by about 20 mmHg in head and 5% in efficiency. Because of the accuracy of our CFD predictions as proven in Figs. 6 and 7, it is reasonable to conclude that the PF4 maglev pump can reach a maximum efficiency  $\sim 27\%$  with human blood (see Fig. 8(b)).

**3.2 Hemolysis.** Shear-induced blood trauma (hemolysis) was evaluated by computing the damage accumulation along 6000 randomly distributed pathlines using a Lagrangian particle tracking technique described previously [14]. The computed overall hemolysis index through the full PF4 flow path over the entire operating range of 0.3–2.3 LPM, at different pump heads and rotor speeds is provided in Fig. 9. The same hemolysis index converted from the benchmark *in vitro* value from PF3 at 1.0 LPM and 16,200 rpm (48 mmHg) is provided for comparison [6]. The blood damage was found to increase with the pump speed and flow rate within the range of 0.3–1.5 LPM, i.e., below the best efficiency point (BEP). From the flow rate of 1.5 to 2.3 LPM, at the same rotor speed of 16,000 rpm, CFD predicted a decrease in blood damage. This unimodal relationship between hemolysis and flow rate has been reported elsewhere [14] and may be attributed to the competing effects of reduced exposure time versus increased fluid stresses. Compared to PF3 *in vitro* hemolysis at 1.0 LPM, the new PF4 design was predicted to have a lower blood damage index of about 0.0032 (versus 0.0058) at the same flow rate but with much greater head (138 mmHg for PF4 versus 48 mmHg for PF3). A further comparison of the two pumps for the same head and flow rate (for instance, 138 mmHg at 1.0 LPM) indicates that PF3 would require at least a  $\sim 40\%$  greater rotor speed than PF4, with correspondingly greater shear stress; thus a much higher hemolysis level than 0.0058.

Further analysis of the contributions of four characteristic regions (Fig. 2(a)) to overall blood damage is shown in Fig. 10. Within the flow range of 0.3–1.0 LPM and the pump speed of 10,000–14,000 rpm, the second-stage axial-flow impeller produced greater hemolysis than that of the first-stage mixed-flow impeller. However, from the flow rate of 1.5–2.0 LPM at 16,000 rpm, the first-stage impeller region produced greater hemolysis than that of the second-stage impeller. At the follow rate of 2.3 LPM and 16,000 rpm, the second-stage region again produced slightly greater hemolysis than that of the first-stage impeller region. It is interesting to note that the contribution by the annular gap region was considerably high in comparison to those by first- and second-stage regions and reached greatest at the flow

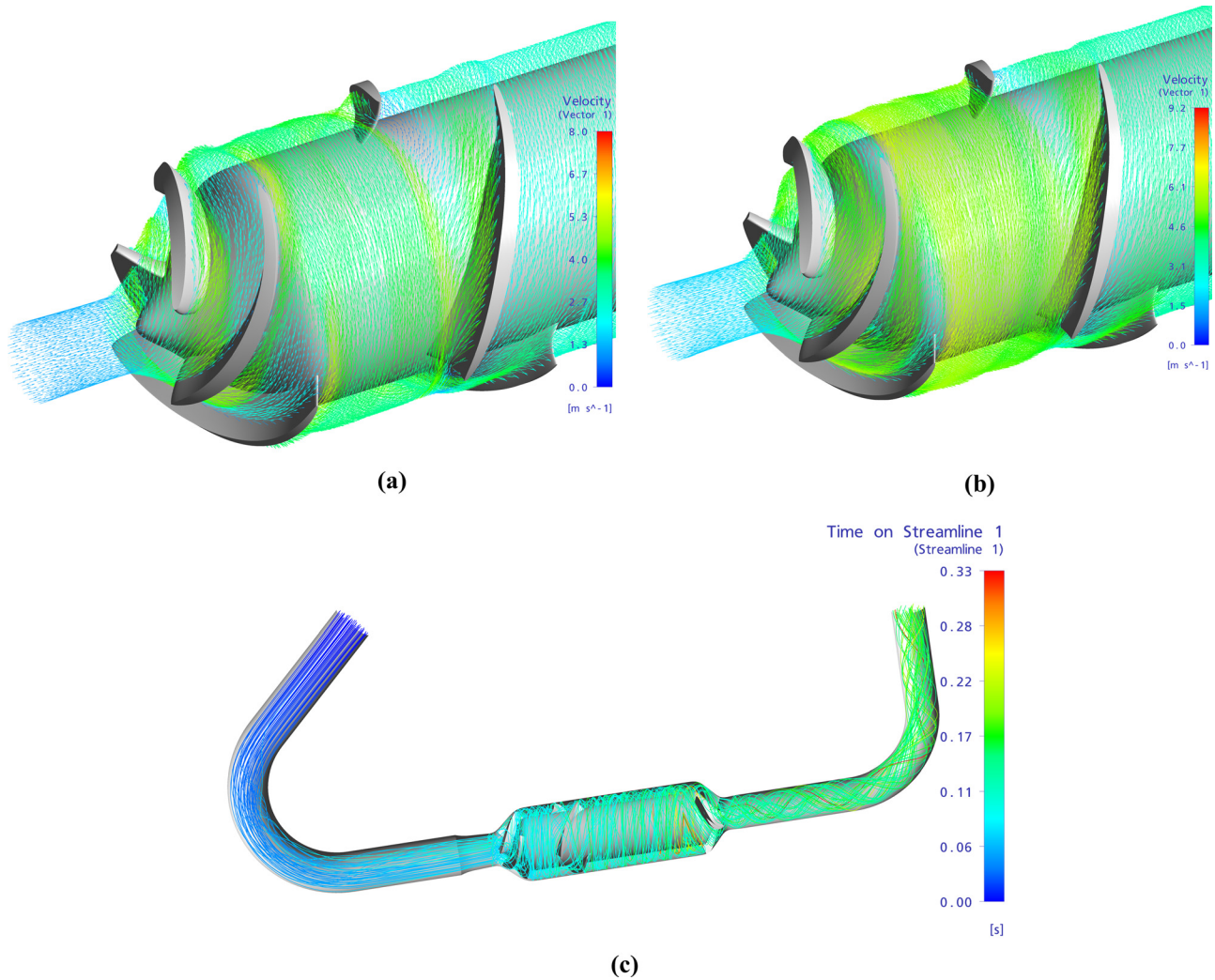


Fig. 5 Predicted flow field at speed = 16,000 rpm. (a) Velocity vectors on mid-span blade-to-blade surface for first- and second-stage impeller ( $Q = 1.5$  LPM). (b) Velocity vectors ( $Q = 2.3$  LPM). (c) Pathlines through PF4 entire flow path ( $Q = 1.5$  LPM).

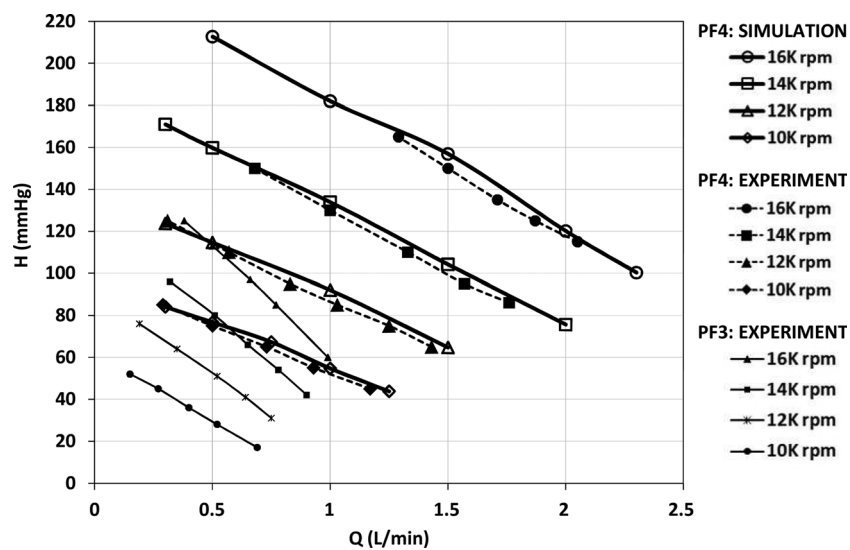


Fig. 6 Comparison of CFD predicted  $H$ - $Q$  results (thick solid lines) with the experimental data for PF4 flow validation fixture (dashed lines). Also superimposed are the experimental data for an equivalent PF3 flow validation fixture (thin solid lines). Analog blood has a density of  $1076 \text{ Kg/m}^3$  and a dynamic viscosity of  $0.0024 \text{ Pa}\cdot\text{s}$ .

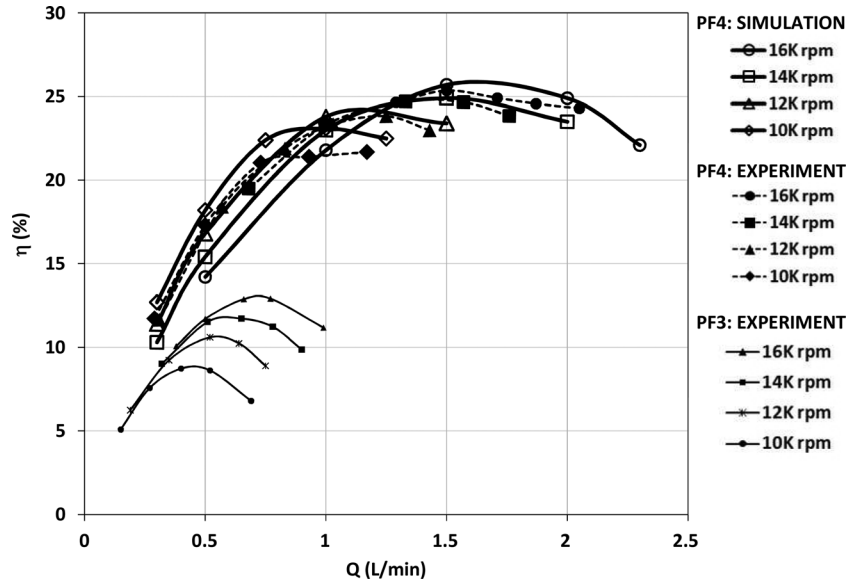


Fig. 7 Comparison of CFD-predicted  $\eta$ - $Q$  results (thick solid lines) with the experimental data for PF4 flow validation fixture (dashed lines). Experimental data for an equivalent PF3 flow validation fixture provided for comparison (thin solid lines). Analog blood has a density of  $1076 \text{ Kg/m}^3$  and a dynamic viscosity of  $0.0024 \text{ Pa}\cdot\text{s}$ .

condition of 1.5 LPM and 16,000 rpm. This indicates again that the annular fluid gap has a significant effect not only on the hydrodynamic performance of the pump but also on the blood trauma. At the flow conditions simulated, the hemolysis contributed by the stator-vane region increased almost exponentially from a flow rate of 0.3–2.0 LPM, and reached a peak at the flow rate of 2.0 LPM and was considerably reduced at 2.3 LPM but dominated the other components. The contributions of the inflow cannula and outflow graft (not shown) were negligible.

**3.3 Fluid Stiffness.** CFD analyses were first performed for three different radial eccentricities of  $50 \mu\text{m}$ ,  $100 \mu\text{m}$ , and  $160 \mu\text{m}$  at the flow rate of 2.3 LPM and rotor speed of 16,000 rpm. At the symmetrical coaxial position, the total radial force acting on the rotor was computed to be zero. With a slight radial eccentricity of the rotor, the pressure distributions at different cross sections of the pump were no longer axisymmetric (see Fig. 11). Unlike conventional journal (squeeze film) bearings with a relatively small clearance to journal diameter ratio, in which the resultant radial

forces tend to restore the rotor to the coaxial position, this large-gap annulus exhibited the opposite effect: producing a destabilizing force in response to radial perturbation. The stiffness calculated from the radial fluid force is defined as *negative fluid stiffness* and competes with the magnetic suspension stiffness, which acts to restore the rotor into the equilibrium coaxial center. Moreover, the unbalanced resultant fluid force has a component orthogonal to the eccentric offset, which is defined as the fluid *cross stiffness* (see Fig. 11). Both the aforementioned stiffnesses can contribute to rotordynamic instability at high flow and high rpm when the fluid forces overwhelm the magnetic suspension forces and fluid damping. The unbalanced radial forces on the rotor were found to exhibit a nearly linear relationship with eccentricity at a given flow rate and rotor speed (results not shown). Such linearity makes it possible to interpolate the negative fluid stiffness by simulating only one radial eccentricity for each flow rate and rotor speed. The influence of flow rate was, however, found to be quadratically related to fluid stiffness at constant rotor speeds (see Fig. 12). The cross stiffness was found to be much

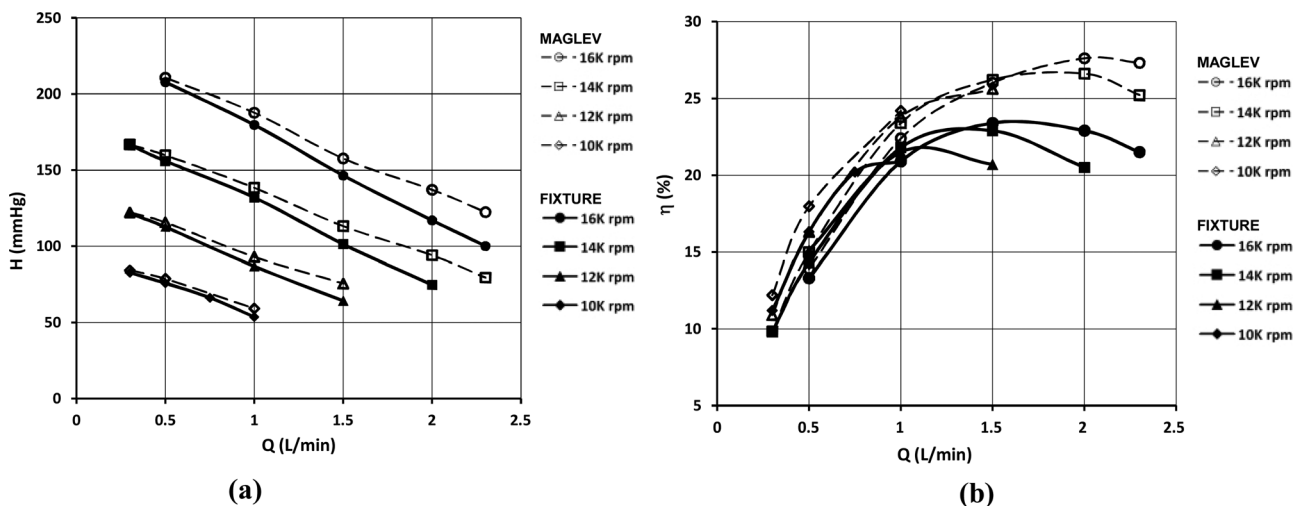


Fig. 8 Comparison of CFD-predicted performance for PF4 flow validation prototype (solid lines), and the maglev model (dashed lines). (a)  $H$ - $Q$  Curves. (b)  $\eta$ - $Q$  Curves. Analog blood has a density of  $1040 \text{ Kg/m}^3$  and a dynamic viscosity of  $0.0035 \text{ Pa}\cdot\text{s}$ .

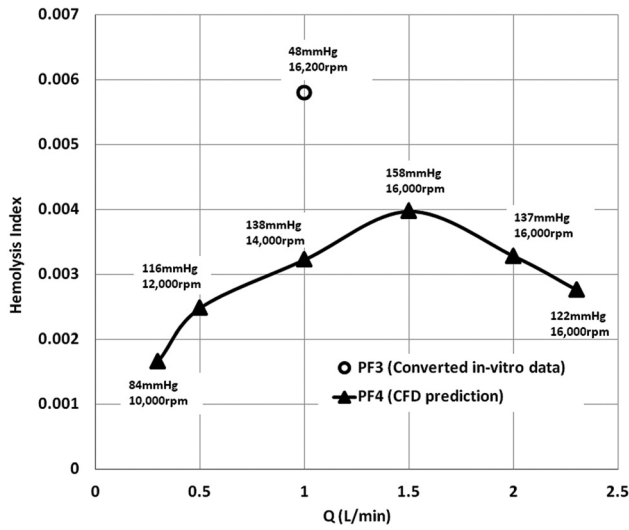


Fig. 9 Computed mean blood damage through the entire PF4 pump model (based on 6000 particles) throughout entire flow range at different pump speeds (and pressure heads). Same hemolysis index converted from *in vitro* data for PF3 at flow rate of 1.0 LPM and pump speed of 16,200 rpm (48 mmHg) shown for comparison.

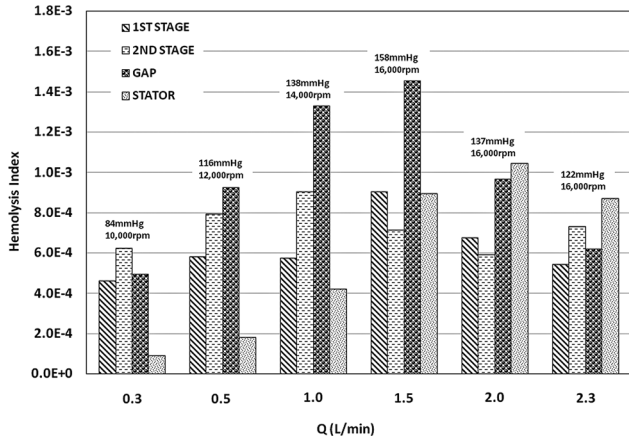


Fig. 10 Portion of total blood damage contributed by different pump components over the entire flow range at different pump speeds and heads.

smaller than that of the radial fluid stiffness and it is not shown here. These CFD predictions provided necessary constraints to design the radial magnetic bearings such that their radial stiffness is guaranteed to overcome that of the negative fluid stiffness over the entire operational range.

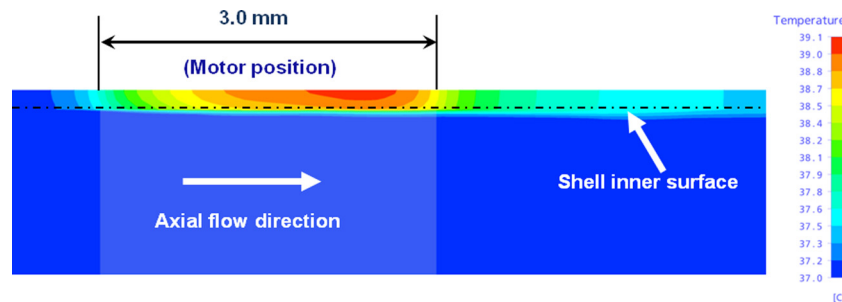


Fig. 13 Predicted temperature distribution on the longitudinal cut-plane (meridional section) at a flow rate of 1.5 LPM and rotor speed of 16,000 rpm. Heat is concentrated within the motor region and dissipated downstream along the shell into a very thin layer of fluid.

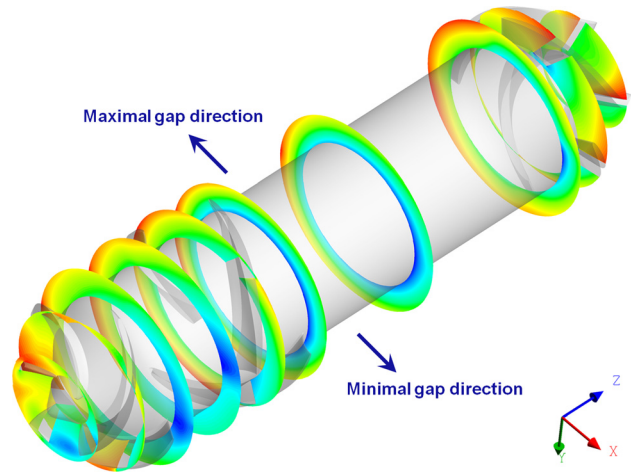


Fig. 11 Pressure contours at different cross sections computed at a radial eccentricity of 160  $\mu\text{m}$  ( $Q=2.3$  LPM and speed = 16,000 rpm)

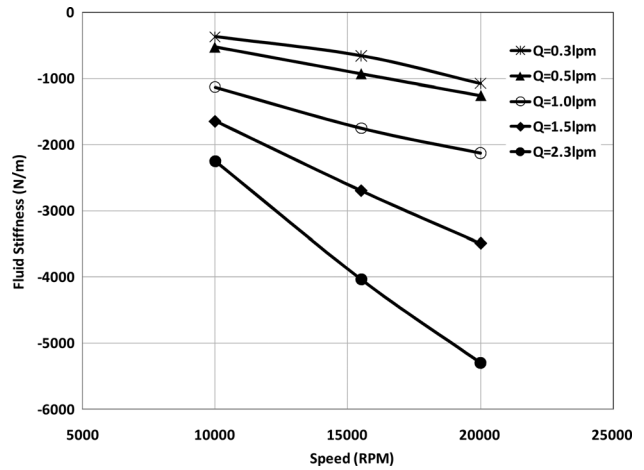
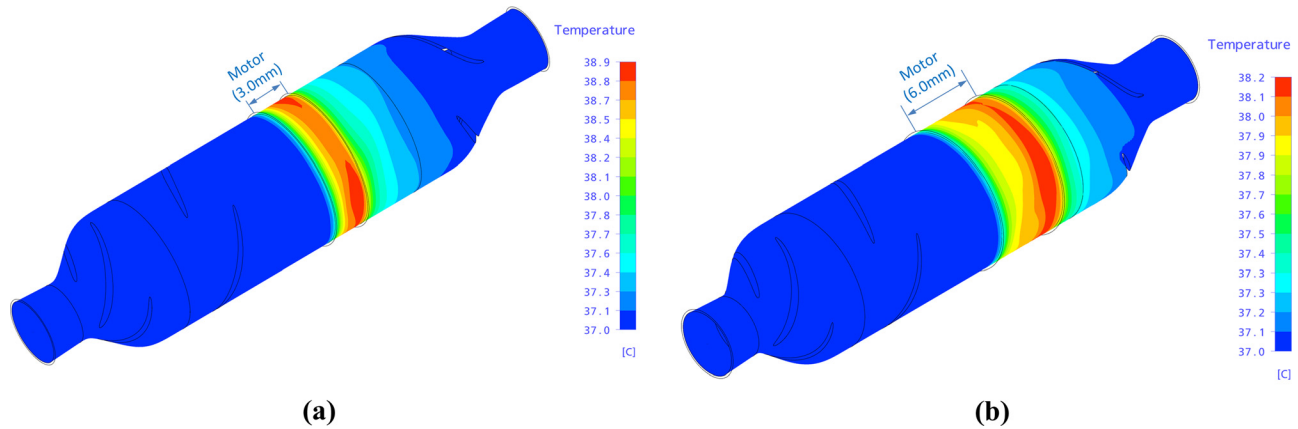


Fig. 12 CFD-predicted negative fluid stiffness as a function of flow rates and rotor speeds

3.4 Thermal Analysis. The predicted temperature on the central cut-plane (meridional section) of the PF4 model with a 3.0mm long motor at the nominal flow condition (1.5 LPM and 16,000 rpm) is illustrated in Fig. 13. The greatest temperature is concentrated near the downstream margin of the motor region and is observed to dissipate downstream along the shell into a very thin layer of blood. Figure 14 further compares the computed temperature distribution on the interface of the titanium shell and



**Fig. 14** Computed temperature distribution on the interface of the titanium shell and flowing blood (flow rate = 1.5 LPM, rotor speed = 16,000 rpm): (a) 3.0-mm-long motor and (b) 6.0-mm-long motor

blood for both the 3.0-mm- and 6.0-mm-long motor at the nominal flow condition. Both cases present similar temperature patterns on the interface which returns to body temperature within approximately 6.0 mm downstream. For the 3.0-mm-long motor (Fig. 14(a)), the maximal temperature rises was  $\sim 2^\circ\text{C}$ . Doubling the motor length (Fig. 14(b)) reduced the maximal temperature to  $\sim 1^\circ\text{C}$ . This analysis provided necessary guidance for the design of the motor for the PediaFlow<sup>®</sup> PF4, specifically in reconciling the tradeoff of size and efficiency to avoid blood thermotrauma.

#### 4 Discussion

CFD-based design optimization has been previously shown to offer far more efficient means of optimization than traditional trial-and-error approaches in the development of a miniature rotodynamic ventricular assist device (VAD) [4,14]. Its utility extends to hemodynamic performance, blood damage and thermo-trauma. This tool was applied here to expedite the re-design of the PediaFlow<sup>®</sup> to improve its performance prior to design freeze.

This study emphasized the importance of computational mesh integrity to achieve accurate results, comparable to experimentation. Unlike commercial grid generation packages, which commonly employ unstructured tetrahedral grids or structured multiblock grids with transfinite interpolation (TFI) and fixed interfaces (such as CFX-TurboGrid) [11], the elliptic automatic mesh generators employed here provided complete continuity over the interfaces through a surrounding layer of phantom points at which values are kept equal to those at corresponding object points inside an adjacent block so that the interfaces are not fixed but are determined automatically by the iteration process [8]. Small O-grids around the blade or vane surfaces with boundary orthogonality and local grid clustering allow accurate prediction of complex flow adjacent to the wall surfaces. The choice of turbulence model used for the simulation is also very important. For the present application having a relatively low Reynolds number, the SST turbulence model provided accurate predictions of  $H-Q$  and  $\eta-Q$  characteristics.

Integration of inverse design approaches with automatic mesh generators has allowed us to readily optimize the pump geometry with respect to a variety of objective functions. For example, hydraulic efficiency,  $\eta$ , may be related to the pump geometric parameters:

$$\eta = f(D_1, D_2, B_i, \beta_1, \beta_2, \theta) \quad (1)$$

where,  $D_1$ ,  $D_2$  are the impeller inlet and outlet mean diameters, respectively;  $B_i$  is the stream-wise blade height;  $\beta_1$  and  $\beta_2$  are the blade leading and trailing edge angles, respectively; and  $\theta$  is the blade wrap angle. Therefore, with any change of the geometric variables provided by inverse design, the automatic mesh genera-

tor provides a smooth, high-quality multiblock structured mesh quickly for repeated CFD simulations until a maximal efficiency,  $\eta$ , can be reached.

A single-stage mixed flow impeller for the first-generation PediaFlow<sup>®</sup> maglev VAD, was previously shown to provide acceptably low blood damage [6], because the high shear stress area along the blade tip region is substantially reduced compared to that of an axial-flow impeller. However, blood discharged from a mixed-flow impeller has relatively greater kinetic energy. Therefore, in the PF3 pump, in which a long axial annular gap separates the impeller from the aft stator vanes, there is significant loss of dynamic head. One remedy might be to position inward-pointed stator vanes immediately after the mixed-flow impeller within the annular gap region. However this is prohibitively difficult to manufacture. An alternate solution, described by Throckmorton et al. [16], is to extend the impeller blades downstream throughout the annulus with a large trailing blade angle. However, this significantly increases the surface area of the blade-tip gap with higher shear stress; thus increasing the risk of blood damage. Moreover, a long axial blade profile is more prone flow separation and vortices between blade-to-blade regions especially at off-design conditions because of the additional length for boundary layer growth [17]. Furthermore, a very large blade trailing angle will increase the reaction ratio (of dynamic to static pressure), which is very undesirable for a blood pump design.

These drawbacks are obviated by the two-stage design of the PF4. Blood flow is directed through the first-stage mixed-flow impeller to obtain both kinetic energy and pressure rise, and then to further gain kinetic energy and pressure head from the second axial-flow impeller region with short camberlines. The two-stage design therefore yields a total greater pump head and efficiency at the same rotor speed than a pure single-stage mixed- or axial-flow configuration. The current two-stage design for PF4 has almost the exact same primary dimensions as the single-stage PF3 design yet exhibited twice the peak hydraulic efficiency, greater head, wider flow range, and lower overall rotor speeds. This provides an excellent demonstration of the power of modern design methods.

Red blood cell damage in rotodynamic blood pumps is mainly caused by elevated shear exposure, particularly along the blade tip clearances, in turn directly related to the rotor speed. Because the two-stage impeller design requires a much lower rotor speed to generate the required head at any given flow rates, it is understandable that the blood damage is decreased, as indicated in Fig. 9. Based on the linear accumulation of blood damage through the blood pump [12], a detailed breakdown analysis of regional contributions to the overall blood damage provided by Wu et al. [14] was further applied to the current study. This regional analysis is useful by providing insights into which components contribute most to the hemolysis level and therefore invite focused optimization.

Negative fluid stiffness has proven to be a critical factor affecting the stable operation of the PediaFlow<sup>®</sup> maglev blood pump. Thus far, no studies have been reported of a numerical method to predict the negative fluid stiffness of a blood pump. This is possibly a result of the complexities involved in mesh generation. For instance, TurboGrid, the commercial mesh generator specially developed for turbomachinery, can only generate the axial-symmetric structured mesh with simple TFI method. Although other commercial mesh generators, such as ICEM-CFD, can generate the tetrahedral grids for a blood pump rotor with eccentricity, the CFD solutions based on a tetrahedral grid are usually less accurate than that of a structured grid [10], and require painstaking efforts to refine the cells in the blade tip gap regions to meet the requirements for the wall-function of turbulence modeling. A further advantage of the automatic mesh generators employed here is their ability to generate a high-quality grid for any radial eccentricities of the rotor by calculating the movement and deformation of vertices in each volume cell based on the existing multi-block structured mesh at the coaxial symmetrical position as shown in Fig. 2. Recent attempts to estimate these forces experimentally have been stifled by the exceptionally small size of the apparatus and its correspondingly low signal-to-noise ratio. Therefore, the CFD simulation results have been indispensable for gaining insights to the mechanisms of instability caused by fluid forces for achieving the desired performance of PF4.

Coupling thermal analysis with fluid dynamics is numerically difficult and time-consuming. In our previous study for the preliminary PediaFlow<sup>®</sup> models, we applied thermal finite element analysis to solve heat transfer in the solid shell and used simple empirical equations for the blood without coupling between the solid and fluid elements [15]. In the current study, the sophisticated fluid-solid coupling technology for thermal analysis yielded solutions for temperature distribution for all regions of interest: the housing shell, motor, and blood within the annulus. These simulations have provided guidance for optimizing the motor design to avoid thermo-trauma.

## 5 Conclusions

A CFD-based design optimization that integrates inverse blade design approaches, automatic mesh generators, and mathematical models of blood trauma with commercial CFD software, has been applied to the miniature rotodynamic PediaFlow<sup>®</sup> pediatric VAD. The final optimized design, the PF4 features a novel impeller having a mixed-flow first stage followed by a short axial-flow second stage. Stator vanes attached to the conical bore of the aft housing provide the final stage of pressure recovery. Extensive CFD simulations and experimental validation of the new optimized PF4 design demonstrates excellent hemodynamic performance with low hemolysis index. Sophisticated CFD analyses for the evaluation of negative fluid stiffness and conjugate heat transfer have helped guide the design optimization at the overall system level. The current studies demonstrate the effectiveness of a CFD-based design approach for evaluation and optimization of hydrodynamic, hemodynamic, and thermal dynamic performance.

## Acknowledgment

This research is supported in part by Contracts HHSN268200448192C, N01-HV-48192 (Pediatric Circular Support); HHSN268201000015C (Pumps for Kids, Infants and Neonates Pre-Clinical Program) from NIHBL/NIH, and Grant R01 HL089456.

## References

- [1] Roger, V. L., Go, A. S., Lloyd-Jones, D. M., Adams, R. J., Berry, J. D., Brown, T. M., Carnethon, M. R., Dai, S., de Simone, G., Ford, E. S., Fox, C. S., Fullerton, H. J., Gillespie, C., Greenlund, K. J., Hailpern, S. M., Heit, J. A., Ho, P. M., Howard, V. J., Kissela, B. M., Kittner, S. J., Lackland, D. T., Lichtman, J. H., Lisabeth, L. D., Makuc, D. M., Marcus, G. M., Marelli, A., Matchar, D. B., McDermott, M. M., Meigs, J. B., Moy, C. S., Mozaffarian, D., Mussolino, M. E., Nichol, G., Paynter, N. P., Rosamond, W. D., Sorlie, P. D., Stafford, R. S., Turan, T. N., Turner, M. B., Wong, N. D., and Wylie-Rosett, J., 2011, "Heart Disease and Stroke Statistics-2011 Update: A Report from the American Heart Association," *Circulation*, **123**(4), pp. e18–e209.
- [2] Moller, J., 1998, "Prevalence and Incidence of Cardiac Malformation," *Perspectives in Pediatric Cardiology: Surgery of Congenital Heart Disease: Pediatric Cardiac Care Consortium, 1984–1995*, Futura Publishing, Armonk, NY, Vol. 6, pp. 19–26.
- [3] Uber, B. E., Webber, S. A., Morell, V. O., and Antaki, J. F., 2006, "Hemodynamic Guidelines for Design and Control of a Turbodynamic Pediatric Ventricular Assist Device," *ASAIO J.*, **52**(4), pp. 471–478.
- [4] Wu, J., Antaki, J. F., Wagner, W., Snyder, T., Paden, B., and Borovetz, H., 2005, "Elimination of Adverse Leakage Flow in a Miniature Pediatric Centrifugal Blood Pump by Computational Fluid Dynamics-Based Design Optimization," *ASAIO J.*, **51**, pp. 636–643.
- [5] Wu, J., Shimmei, K., Tani, K., Niiura, K., and Sato, J., 2007, "CFD-Based Design Optimization for Hydro Turbines," *ASME J. Fluids Eng.*, **129**(2), pp. 159–168.
- [6] Maul, T., Antaki, J. F., Wu, J., Kim, J., Kameneva, M., Olia, S., Wearden, P., Kocylidirim, E., and Borovetz, H., 2011, "In Silico Design and in Vivo Analysis of the PediaFlow<sup>TM</sup> Pediatric Ventricular Assist Device," Proceedings of the ASME Summer Bioengineering Conference, June 22–25, Namacolin Woodlands, Pennsylvania, USA.
- [7] Antaki, J. F., Ricci, M., Verkaik, J., Snyder, S., Maul, T., Kim, J., Paden, D., Kameneva, M., Paden, B., Wearden, P., and Borovetz, H., 2010, "PediaFlow Maglev Ventricular Assist Device: A Prescriptive Design Approach," *Cardio-vasc. Eng. Technol.*, **1**(1), pp. 104–121.
- [8] Thompson, J., Soni, B., and Weatherill, N., 1999, *Handbook of Grid Generation*, CRC Press, Boca Raton, FL.
- [9] Stepanoff, A. J., 1966, *Centrifugal and Axial Flow Pumps: Theory, Design, and Application*, John Wiley & Sons, New York.
- [10] Ferziger, J. H., and Perić, M., 2002, "Computational Methods for Fluid Dynamics," Springer, New York.
- [11] ANSYS, Inc., CFX ANSYS, 2010, "User's Guide."
- [12] Bludszwejt, C., 1995, "Model for a General Mechanical Blood Damage Prediction," *Artif. Organs*, **19**, pp. 583–519.
- [13] Song, X., Throckmorton, A. L., Antaki, J. F., and Olsen, D. B., 2004, "Quantitative Evaluation of Blood Damage in a Centrifugal VAD by Computational Fluid Dynamics," *ASME J. Fluids Eng.*, **126**(3), pp. 410–419.
- [14] Wu, J., Paden, B., Borovetz, H., and Antaki, J. F., 2009, "Computational Fluid Dynamics Analysis of Blade Tip Clearances on Hemodynamic Performance and Blood Damage in a Centrifugal Ventricular Assist Device," *Artif. Organs*, **34**(5), pp. 402–411.
- [15] Gardiner, J., Wu, J., Noh, M., Antaki, J. F., Snyder, T., Paden, D., and Paden, B., 2007, "Thermal Analysis of the Pediatric Ventricular Assist Device," *ASAIO J.*, **53**, pp. 65–73.
- [16] Throckmorton, A., Untaroiu, A., Allaire, P., Wood, H., Matherne, G. P., Lim, D., Peeler, B., and Olsen, D., 2004, "Computational Analysis of an Axial Flow Pediatric Ventricular Assist Device," *Artif. Organs*, **28**(1), pp. 881–891.
- [17] Wu, Z., Antaki, J. F., Burgreen, G. W., Butler, K. C., Thomas, D. C., and Griffith, B. P., 1999, "Fluid Dynamic Characterization of Operating Conditions for Continuous Flow Blood Pumps," *ASAIO J.*, **45**(5), pp. 442–449.